The Astrophysical Journal, 583:70–84, 2003 January 20
© 2003. The American Astronomical Society. All rights reserved. Printed in U.S.A.

CHANDRA SPECTRA OF THE SOFT X-RAY DIFFUSE BACKGROUND

M. Markevitch, M. W. Bautz,[1] B. Biller, Y. Butt, R. Edgar, T. Gaetz, G. Garmire,[2] C. E. Grant,[1]
P. Green, M. Juda, P. P. Plucinsky, D. Schwartz, R. Smith, A. Vikhlinin, S. Virani,
B. J. Wargelin, and S. Wolk
Harvard-Smithsonian Center for Astrophysics, 60 Garden Street, Cambridge, MA 02138; maxim@head-cfa.harvard.edu
Received 2002 June 25; accepted 2002 October 2

ABSTRACT

We present an exploratory *Chandra* ACIS-S3 study of the diffuse component of the cosmic X-ray background (CXB) in the 0.3–7 keV band for four directions at high Galactic latitudes, with emphasis on details of the ACIS instrumental background modeling. Observations of the dark Moon are used to model the detector background. A comparison of the Moon data and the data obtained with ACIS stowed outside the focal area showed that the dark Moon does not emit significantly in our band. Point sources down to 3×10^{-16} ergs s^{-1} cm^{-2} in the 0.5–2 keV band are excluded in our two deepest observations. We estimate the contribution of fainter, undetected sources to be less than 20% of the remaining CXB flux in this band in all four pointings. In the 0.3–1 keV band, the diffuse signal varies strongly from field to field and contributes between 55% and 90% of the total CXB signal. It is dominated by emission lines that can be modeled by a $kT = 0.1$–0.4 keV plasma. In particular, the two fields located away from bright Galactic features show a prominent line blend at $E \approx 580$ eV (O VII+O VIII) and a possible line feature at $E \sim 300$ eV. The two pointings toward the North Polar Spur exhibit a brighter O blend and additional bright lines at 730–830 eV (Fe XVII). We measure the total 1–2 keV flux of $(1.0$–$1.2 \pm 0.2) \times 10^{-15}$ ergs s^{-1} cm^{-2} arcmin^{-2} (mostly resolved) and the 2–7 keV flux of $(4.0$–$4.5 \pm 1.5) \times 10^{-15}$ ergs s^{-1} cm^{-2} arcmin^{-2}. At $E > 2$ keV, the diffuse emission is consistent with zero, to an accuracy limited by the short Moon exposure and systematic uncertainties of the S3 background. Assuming Galactic or local origin of the line emission, we put an upper limit of $\sim 3 \times 10^{-15}$ ergs s^{-1} cm^{-2} arcmin^{-2} on the 0.3–1 keV extragalactic diffuse flux.

Subject headings: intergalactic medium — ISM: general — methods: data analysis — X-rays: diffuse background — X-rays: ISM

1. INTRODUCTION

The existence of a cosmic X-ray background (CXB) was one of the first discoveries of extrasolar X-ray astronomy (Giacconi et al. 1962). In the intervening four decades, observations with improving angular and spectral resolution have enhanced our understanding of the components that make up this background. Several broadband, all-sky surveys have been performed using proportional counter detectors (Marshall et al. 1980; McCammon et al. 1983; Marshall & Clark 1984; Garmire et al. 1992; Snowden et al. 1995, 1997; for a review of pre-*ROSAT* results, see McCammon & Sanders 1990). These surveys form a consistent picture of the angular distribution of X-ray emission in the various bands. Above 2 keV, the emission is highly isotropic on large angular scales and has an extragalactic origin. Below 2 keV, the X-ray background is a mixture of Galactic diffuse emission (see, e.g., Kuntz & Snowden 2000 and references therein), heliospheric and geocoronal diffuse components (see, e.g., Cravens 2000), and extragalactic flux from point sources and, possibly, from intergalactic warm gas that may contain the bulk of the present-day baryons (see, e.g., Cen & Ostriker 1999).

The earliest observations could provide only limited spectral information on the background. Marshall et al. (1980) found that the spectrum in the 3–50 keV range was well fitted by a thermal bremsstrahlung model with $kT \sim 40$ keV. In the 3–10 keV band, this can be approximated by a power law with a photon index of -1.4. At energies below 1 keV, the background surface brightness exceeds the extrapolation of this power law (Bunner et al. 1969). Later observations with gas scintillation proportional counters and solid-state detectors (Inoue et al. 1979; Schnopper et al. 1982; Rocchia et al. 1984) suggested emission lines in the 0.5–1.0 keV band, most likely from oxygen. The evidence for emission lines in this band has become more convincing in recent observations using CCDs (Gendreau et al. 1995; Mendenhall & Burrows 2001) and in a high-resolution spectrum obtained by McCammon et al. (2002) in a microcalorimetric experiment. A definitive demonstration of spectral lines in the 0.15–0.3 keV band (at low Galactic latitude) was obtained by Sanders et al. (2001), using a Bragg crystal spectrometer. Observations that combine high spectral and angular resolution are essential for disentangling the many CXB soft emission components.

Chandra and *XMM* should soon provide a wealth of new information on the CXB. Several works have already taken advantage of the *Chandra*'s arcsecond resolution to study the point-source component of the CXB (see, e.g., Mushotzky et al. 2000; Brandt et al. 2001; Rosati et al. 2002). The first *XMM* results are starting to appear as well (De Luca & Molendi 2002; Warwick 2002; Lumb et al. 2002), utilizing the large effective area of that observatory.

In this paper, we present a *Chandra* ACIS study of the diffuse CXB at high Galactic latitudes. The main advantage of *Chandra* over all other instruments is its ability to resolve point sources down to very low fluxes and probe the true dif-

[1] Center for Space Research, Massachusetts Institute of Technology, Cambridge, MA 02139.

[2] Department of Astronomy and Astrophysics, Pennsylvania State University, 525 Davey Laboratory, University Park, PA 16802.

fuse background. In addition to that, compared to *ROSAT* PSPC (which had lower detector background), ACIS has energy resolution sufficient to identify spectral lines. Compared to *XMM* EPIC, ACIS appears to be less affected by instrumental background flares (although during quiescent periods, the ACIS detector background per unit sky signal is higher). To the extent that results can be compared, we confirm many of the recent findings made with other instruments.

Technical aspects of our study, especially the ACIS instrumental background modeling, are quite complex, and we discuss them here in detail. Much of our analysis procedure may be useful for studies of extended sources such as clusters of galaxies. Uncertainties are 1 σ unless specified otherwise.

2. DATA SET

For this exploratory study of the diffuse CXB, we selected four *Chandra* ACIS-S observations at high Galactic latitudes, listed in Table 1. Our main focus is two relatively deep (90–100 ks) observations, observation IDs (ObsIDs) 3013 and 3419, obtained at positions away from any bright Galactic features seen in the RASS (*ROSAT* All-Sky Survey) R4–R5 ($\frac{3}{4}$ keV) band (Snowden et al. 1997). For comparison, we also analyze two shorter archival observations toward an edge (ObsID 869) and the middle (ObsID 930) of the North Polar Spur,[3] which exhibits bright emission in the *ROSAT* R4–R5 band. In Figure 1, positions of the four observations are overlaid on the RASS R4–R5 map. None of these observations' original goals were related to CXB, and there are no nearby cataloged extended sources, except an irregular galaxy that was a target of ObsID 869 and is spatially excluded from our analysis.

3. ACIS INSTRUMENTAL BACKGROUND

A critical part of this study is modeling of the ACIS instrumental background. This background is caused by cosmic charged particles and consists of a slowly changing quiescent component and at least two species of highly variable background flares, whose spectra are very different from that of the quiescent component. Below we describe in detail how these components were dealt with from a practical perspective; their exact physical nature is beyond the scope of this paper.

[3] The North Polar Spur, part of the Loop I supershell of emission in the RASS (Egger & Aschenbach 1995), is thought to be the collision of explosive remnants with the Local Bubble.

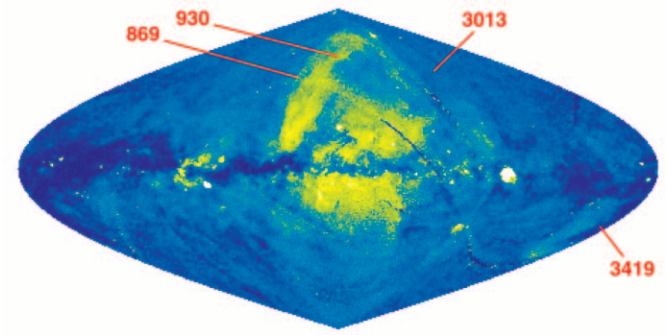

FIG. 1.—*ROSAT* PSPC all-sky map of CXB in the R4–R5, or $\frac{3}{4}$ keV, band (Snowden et al. 1997), in Galactic coordinates. Positions of our observations are marked; labels give ObsIDs.

3.1. *Background Flare Filtering*

We use data from the ACIS back-side–illuminated (BI) chip S3. Compared to the ACIS front-side–illuminated (FI) chips, S3 has a higher sensitivity at low energies. However, its sensitivity to low-energy X-rays also renders it more sensitive to particle events, which results in more frequent background flares than in FI chips (Plucinsky & Virani 2000; Markevitch 2001[4]). The quiescent background is stable and predictable; therefore, when the accuracy of the background subtraction is critical, it is best to exclude flare periods from the analysis. The spectra of the flaring and quiescent background components (discussed below) are such that the best energy band in which to look for flares in chip S3 is approximately 2.5–7 keV. Figure 2 shows light curves in this energy band for our four observations (from the whole S3 chip, excluding celestial sources). The time bin size ($\sim$1 ks) is chosen to limit the statistical scatter while providing a reasonably detailed light curve.

In observations 3419, 869, and 930, the quiescent rate is easily identifiable and very close to that in most other observations performed during 2000–2001. To limit the background modeling uncertainty, we exclude from further analysis all time bins above and below a factor of 1.2 of this rate (the rate can be lower, for example, because of occasional short intervals of missing telemetry and bad aspect, etc.). The resulting clean exposures are given in Table 1.

3.1.1. *Anomalous Background in Field* 3013

Observation 3013 is unusual in that the apparent "quiescent" rate between the numerous flare intervals (Fig. 2) is about 30% higher than in other observations. It is also more variable than the quiescent rate usually is. It appears that, in fact, all of this exposure is affected by a long flare, which requires special treatment (and, unfortunately, will add to the systematic uncertainty of the results).

Again, we exclude the time periods above a factor of 1.2 of the apparent quiescent rate. Assuming that the background excess in the rest of the exposure is indeed a flare, we can try to model it by taking advantage of the empirical finding, based on a number of observations, that the spectral shape of the most frequent, "soft" species of the BI flares stays the same even while their flux varies strongly in time. To illustrate this, we derive spectra of the background flare components from the rejected, high count rate periods of observations 3013 and 930. We first check the light curves of FI chips also used in these observations, in order to exclude flares of a different, "hard" species that is less frequent, affects both the BI and FI chips, and has a different spectrum. There are 1–2 ks of such flares within the already excluded time periods in each observation. After excluding those, we extract the spectra from the remaining high-rate periods and subtract from them the spectra of the quiescent periods of the same observations, normalizing them by the respective exposure ratios (thereby subtracting all

[4] For Markevitch (2001), see http://asc.harvard.edu/cal, sections "ACIS," "Background," "General discussion."

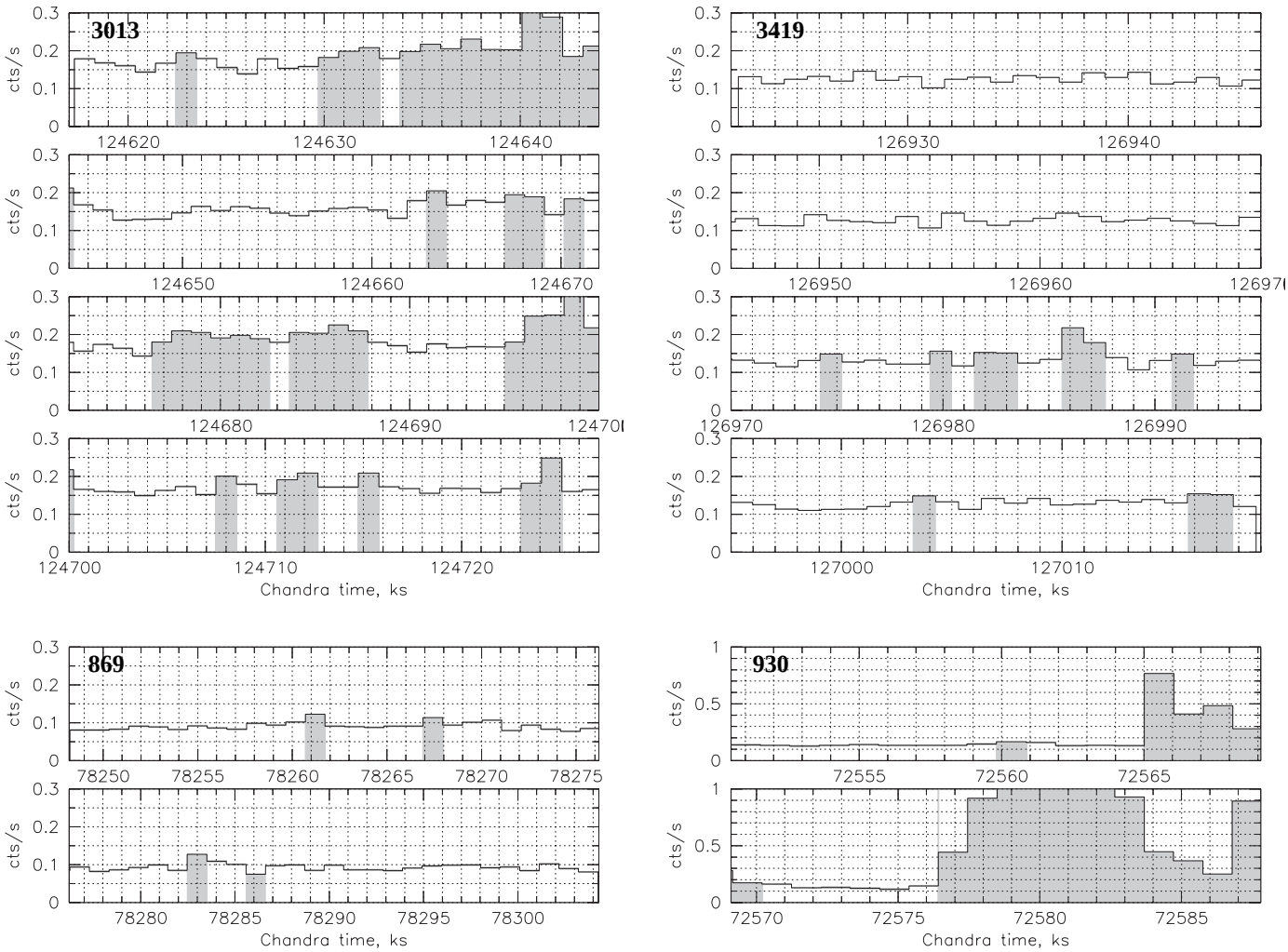

Fig. 2.—Light curves of the four CXB observations in the 2.5–7 keV band, where the contribution of flares is most easily detected. ObsIDs are marked in each panel. For ObsID 869, only 72% of the chip area is used. Very Faint mode filtering was applied (§ 3.3). Shaded bins are above or below a factor of 1.2 of the quiescent level and are excluded.

time-independent sky and instrumental background components). The resulting flare spectra are shown in Figure 3.

In a similar manner, we also extracted flare spectra from several other archival observations (ObsIDs 766, 326, 2206, 2076, 2213, and 1934) spanning a period 2000 February–2001 September and a range of flare intensities. Flares in all those observations can be described by a model consisting of a power law with a photon index of −0.15 and an exponential cutoff at 5.6 keV, without the application of the telescope effective area and the CCD quantum efficiency (commands *arf none* or *model/b* in XSPEC). In Figure 3, this model is overplotted on the flare spectra from our CXB fields 930 and 3013, fixing the spectral shape and fitting only the normalization. As the figure shows, flares in both our observations have nearly the same spectral shape, despite their time difference of 1.5 yr and very different intensities.

TABLE 1
Data Summary

Parameter	ObsID 3013	ObsID 3419	ObsID 869	ObsID 930	Moon
(l, b) (deg)	(259.6, +56.9)	(187.1, −31.0)	(36.6, +53.0)	(358.7, +64.8)	...
Galactic $N_{\rm H}$ ($\times 10^{20}$ cm^{-2})	4.1	11.4	4.3	1.8	...
ROSAT R4–R5 flux ($\times 10^{-6}$ counts s^{-1} arcmin^{-2})	160	90	200–250[a]	400	...
Observation date	2001 Dec 13	2002 Jan 8	2000 Jun 24	2000 Apr 19	2001 Jul 26
Total (uncleaned) exposure (ks)	112	98	57	40	16
Exposure for source detection (ks)	101	92	52	28	...
Exposure for CXB spectra (ks)	69	86	52	20	11
Field solid angle (arcmin^2)	69	69	51	69	70

[a] Affected by an artifact in the *ROSAT* all-sky map.

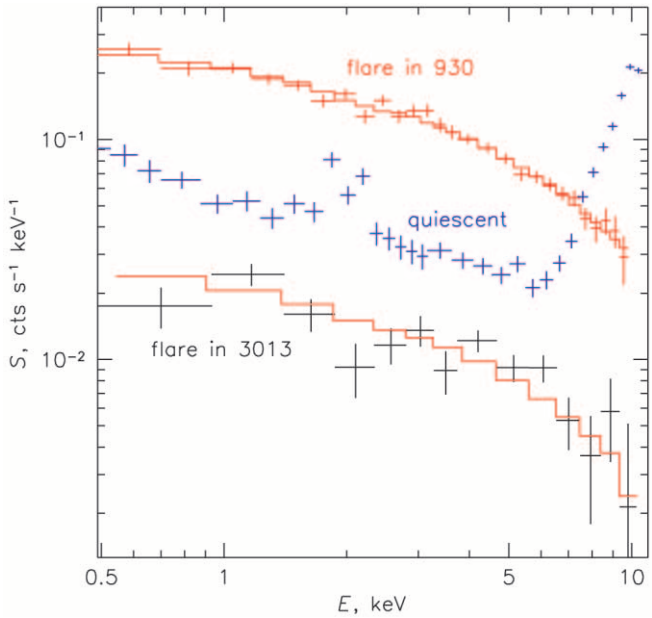

FIG. 3.—Spectra of the excluded background flares (see text) in ObsIDs 930 (*red*) and 3013 (*black*), compared to the quiescent spectrum from the dark Moon (*blue*), for the whole S3 chip. Red histograms show a model that was fitted to a combination of other observations with flares and renormalized, without a change of shape, to match the ObsID 930 and 3013 spectra.

Freeing the spectral shape parameters, we obtained a photon index of -0.10 ± 0.07 and a cutoff at 5.2 ± 0.7 keV for observation 930 and -0.1 ± 0.3 and $7.2^{+\infty}_{-3.4}$ keV for 3013, consistent with the above fit for the composite flare spectrum.

Therefore, if the background excess affecting the useful period of observation 3013 is indeed a residual flare, we can expect that it has the same spectral shape, only a still lower normalization. As is seen in § 6, its spectrum is indeed consistent with this assumption at the energies for which the comparison is possible. To try modeling the residual background excess in 3013, we chose to fix the shape parameters to the best-fit values from this particular observation (given above), even though they are less strongly constrained than those from the composite spectrum, to account for any possible slow evolution of the spectrum, which cannot be ruled out with the data at hand. This choice has no significant effect on our results. The normalization of this flare model is determined in § 6, after subtraction of the quiescent background component and removal of point sources.

For comparison, Figure 3 also shows a quiescent instrumental background spectrum from the dark-Moon observations (discussed below). We note that the BI soft flare spectrum at high energies is much softer than the quiescent background; unless the flare is very strong, its contribution above 10 keV is unnoticeable (this is not true for the other, hard flare species mentioned above). This fact is used below.

3.2. *Quiescent Background*

3.2.1. *Dark-Moon Observations*

To separate the CXB and instrumental components of the ACIS background, *Chandra* observed the dark Moon in 2001 July in a series of six short pointings (ObsIDs 2469, 2487, 2488, 2489, 2490, and 2493), tracking the Moon for a total of about 15 ks. ACIS chips S2, S3, I2, and I3 were on and telemetered data in Very Faint (VF) mode. A second installment of Moon observations in 2001 September exposed chips I2 and I3. Technical difficulties encountered in these two runs, related mostly to the fact that the *Chandra* aspect camera cannot be used near the Moon, prevented further dark-Moon observations. Here we use only the S3 data from 2001 July. During that run, optical flux from the $\frac{1}{3}$ of the lunar disk that was illuminated was imaged onto to the ACIS focal plane. The ACIS optical blocking filters were not designed to reject visible light from the sunlit Moon, and a detectable offset signal (bias error) was produced. The effect was most severe in chip I2, but very small in chip S3. A correction to each event's pulse-height amplitude (PHA) was calculated individually by averaging the lowest 16 pixels of the 5×5 pixel VF mode event island. This offset in S3 was well below the threshold of affecting the event grades, so this problem did not result in any loss of events due to the onboard grade rejection (as was the problem for chip I2 in this data set). The average correction to the energy for events in chip S3 was within a few eV, negligible for our purposes.

A 2.5–7 keV S3 light curve for all 2001 July dark-Moon observations is shown in Figure 4. The end of the exposure was affected by an apparent faint flare, which was filtered using the same factor of 1.2 threshold as in § 3.1 (we had to use smaller time bins, which resulted in some statistical deviations that were also excluded for consistency). The resulting clean Moon exposure for S3 is 11,400 s. At high energies, where the CXB contribution is negligible, the Moon quiescent background rate was within a few percent of that in other recent observations. Scientific results from the Moon observations will be discussed by C. E. Grant et al. (2003, in preparation).

3.2.2. *Event Histogram Mode Data*

An independent approach to calibrating the ACIS instrumental background utilizes the event histogram mode (EHM) data (Biller, Plucinsky, & Edgar 2002).[5] These data are collected during science observations by the HRC-I detector while ACIS is stowed inside the detector support structure. This structure blocks celestial X-rays but does not affect the particle rate significantly (as is seen below). In this mode, the telemetry capacity available for ACIS is small, so the only information transmitted is a PHA histogram for the events from a predefined region of the chip. For this reason, the usual exclusion of bad pixels and the position-dependent gain correction cannot be applied. At this location, ACIS is also faintly illuminated by the internal

[5] See http://asc.harvard.edu/cal, sections "ACIS," "Background," "Event Histogram mode."

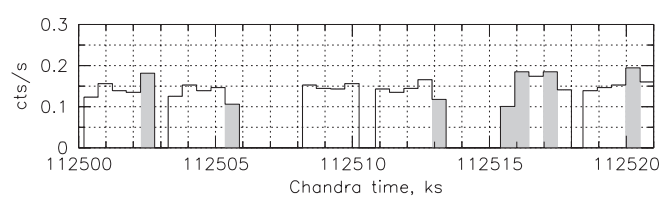

FIG. 4.—Same as Fig. 2, but for the 2.5–7 keV light curve for the dark-Moon observations. The rate is shown before VF mode filtering (§ 3.3).

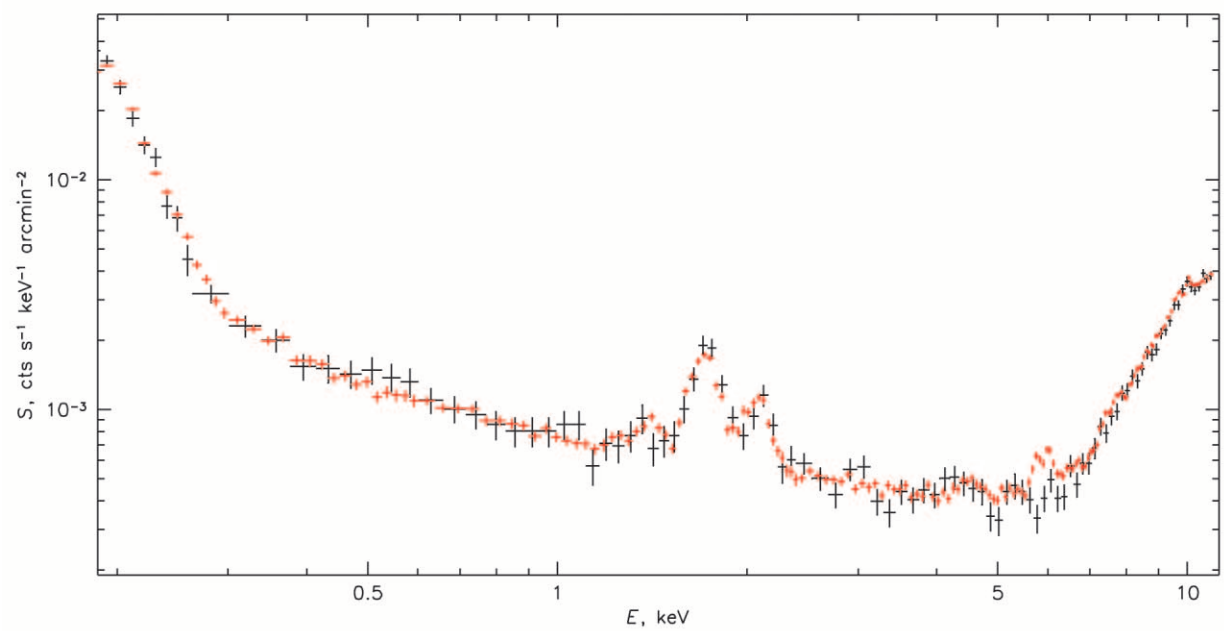

FIG. 5.—Spectra of dark-Moon (*black*) and EHM data (*red*). This Moon spectrum is extracted in PHA channels in a special manner to be directly comparable to the EHM data (see text). The energy scale is approximate (PHA values multiplied by 4.7 eV per channel). Apart from the faint internal calibration source lines present in the EHM data (most notably at 5.9 and 1.5 keV), there is very good agreement between the spectra.

calibration line source. The flare component discussed in § 3.1 is never observed in the stowed position.

An EHM spectrum from the whole S3 chip accumulated over the 2001 July–October period (straddling the date of the Moon observation) is shown in Figure 5 (see also Biller et al. 2002). For comparison, we overlaid a dark-Moon spectrum. In order for it to be directly comparable to the EHM spectrum, in deriving it we did not exclude bad CCD pixels, apply gain corrections (that is, we used PHA rather than pulse height invariant, or PI, values), or apply the additional VF mode filtering (§ 3.3).

Figure 5 shows that away from the calibration source lines, the agreement between the spectra is quite remarkable over the entire energy range, within the statistical accuracy of the Moon data set. One might expect both the dark-Moon and the EHM spectra to exhibit emission above the non–cosmic background level seen in ordinary observations; e.g., *ROSAT* and *ASCA* Moon data suggested emission at low energies (Schmitt et al. 1991; Kamata et al. 1999), and the detector support structure may be radioactive. In principle, one could also imagine a component of the quiescent particle background that can be blocked by that structure. While the coincidence of the two spectra in Figure 5 does not rule out a conspiracy of these possibilities, it makes each of them very unlikely. It also supports the conclusion by Freyberg (1998) that the *ROSAT* emission in the direction of the dark Moon was actually fluorescent emission from a region around the Earth (i.e., below the *Chandra* orbit). Therefore, we assume that both the dark-Moon and the EHM data give the true quiescent background, and we use the Moon data set as an instrumental background model for the sky data below.

The EHM data were also used directly as the background model for a CXB study by R. J. Edgar et al. (2003, in preparation). Another measure of the ACIS background was obtained in 1999 August, just prior to opening the *Chandra* telescope door. That data set is analyzed in Baganoff (1999), which may be consulted for background line identifications and other qualitative information.[6] Unfortunately, those data cannot be used directly for recent observations, because both the background and the ACIS detector have evolved significantly since then. Forthcoming calibration observations with ACIS stowed and working in the full imaging mode (as opposed to EHM), could be used for the most recent observations.

3.2.3. *Background Time Dependence*

From the analysis of a large number of ACIS observations and monitoring of the rate of ACIS events rejected on board (Grant, Bautz, & Virani 2002), we know that the high-energy quiescent background slowly declined from launch until around the end of 2000 and has been relatively constant during 2001 (Fig. 6 shows this behavior in the 5–10 keV band, where the instrumental background dominates), in anticorrelation with the solar cycle. At low energies, the qualitative behavior is similar, but it is difficult to tell exactly because of the differing sky signal. In addition to the slow evolution, there are small variations of the quiescent rate on short timescales. Since the background can change between the observations of our fields and the Moon, the Moon background may need a correction, and the background uncertainty must be included in the final results.

The EHM data are free from the sky signal and flares and can be used for checking the quiescent background time dependence, especially in the soft band most important for the present study. From the comparison of EHM (as well as blank-field) data in different energy bands, it appears that during the short-term quiescent background fluctuations, such as those in Figure 6, its spectral shape does not change significantly and only the normalization varies. This behav-

[6] See http://asc.harvard.edu/cal, sections "ACIS," "Background," "Measurement with closed mirror cover."

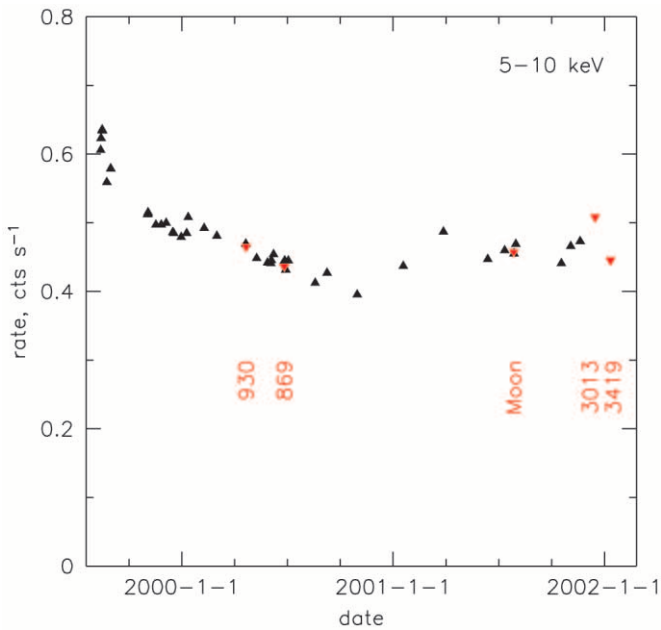

FIG. 6.—Time dependence of the S3 chip 5–10 keV quiescent background rate in various blank-field observations since launch (see Markevitch 2001). Statistical errors are comparable to the symbol size. Red symbols denote observations used in this work (ObsID 3013 is shown before the residual flare correction).

ior enables us to account for these variations by normalizing the model instrumental background by the ratio of rates at high energies, e.g., 10–12 keV, where the contribution from celestial sources and possible faint undetected flares (§ 3.1.1) is negligible.

Figure 7 shows EHM rates from the full S3 chip in the 0.5–2, 2–7, and 5–10 keV bands divided by the rates in the PHA interval of 2500–3000 ADU (approximately 10–12 keV; PHA is preferred over energy because many science observations use an onboard cutoff at 3000 ADU). The period from 2001 July is shown because earlier EHM data were collected from parts of the chip. The scatter of these ratios is quite small; in all energy bands, the intrinsic scatter around the mean required in addition to the Poissonian scatter is 1.5%–2% (1 σ) or less, a reduction from 3%–4% for fluxes not normalized by the high-energy rate. One also notices that neither the rates nor the spectral shape changed systematically between the dates of the Moon observation and our deep observations 3013 and 3419.

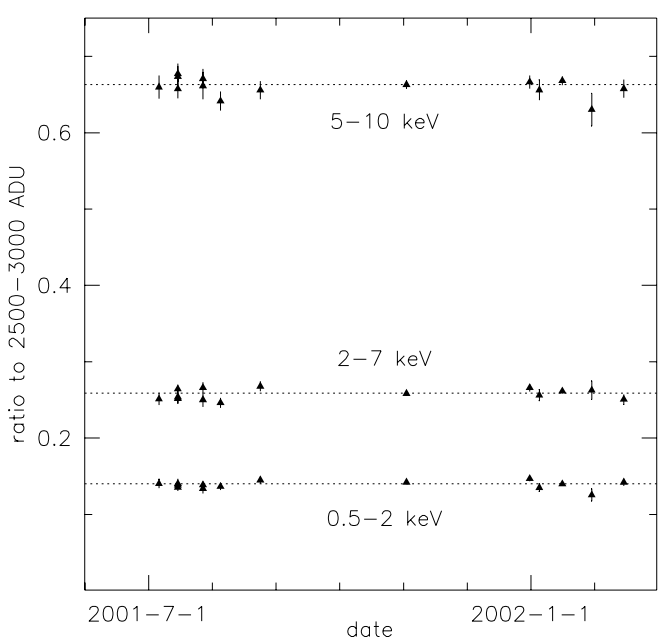

FIG. 7.—Ratios of the S3 background rates in the 0.5–2, 2–7, and 5–10 keV bands to the 2500–3000 ADU (~10–12 keV) rate, for EHM observations that used the full chip. Horizontal lines show average values.

We use such high-energy rate matching in our CXB analysis by normalizing the Moon spectrum by the ratio of the respective 2500–3000 ADU rates. For ObsIDs 3013, 3419, 930, and 869, such normalizations are 1.06, 0.97, 1.01, and 0.93 times the ratio of the Moon exposure to the respective exposures, so this correction is, as expected, small. We adopt a systematic uncertainty of the resulting quiescent background normalization of 2% (1 σ), as derived above.

We note that over longer periods, the spectral shape of the detector background can change—the spectra of the empty-field observations from 2000 and 2001 differ by ~5% at energies where the noncosmic component dominates. This means that the Moon spectrum with a simple normalization adjustment might not be a good model for our earlier observations 930 and 869. However, as seen below, the soft diffuse signal in those observations is so strong that the background uncertainty does not matter.

3.3. *VF Mode Background Filtering*

In VF ACIS telemetry mode, the detector background can be reduced significantly by rejecting events with signal above the split threshold in any of the outer pixels of the 5×5 pixel event island, after an approximate correction for the charge transfer inefficiency. Details of the method can be found in Vikhlinin (2001).[7] Figure 8 shows the effect of such filtering on the spectra of the background (the dark Moon) and real X-ray events from an extended celestial source unaffected by photon pileup. It results in a significant reduction of the background rate, especially at the lowest and highest energies, while rejecting only about 2% of the real events. The background reduction is stronger for FI chips (not used in this work). All four of our CXB observations, as well as all Moon observations, were telemetered in VF mode and filtered in this manner.

4. POINT SOURCES

We now detect and exclude point sources in our CXB fields. All of the S3 chip is within 7′ of the optical axis, and the point-spread function (PSF) is narrow over the whole field, so point-source detection is photon-limited and background is relatively unimportant for it. It is therefore advantageous to include periods of moderately high background if it significantly increases the exposure. For observations 3013, 3419, and 930, we applied a less restrictive light-curve filtering (using the 0.3–10 keV band, and for 930 a higher threshold factor of 2, instead of 1.2) to increase the exposures for source detection (see Table 1).

[7] See http://asc.harvard.edu/cal, sections "ACIS," "Background," "VF mode."

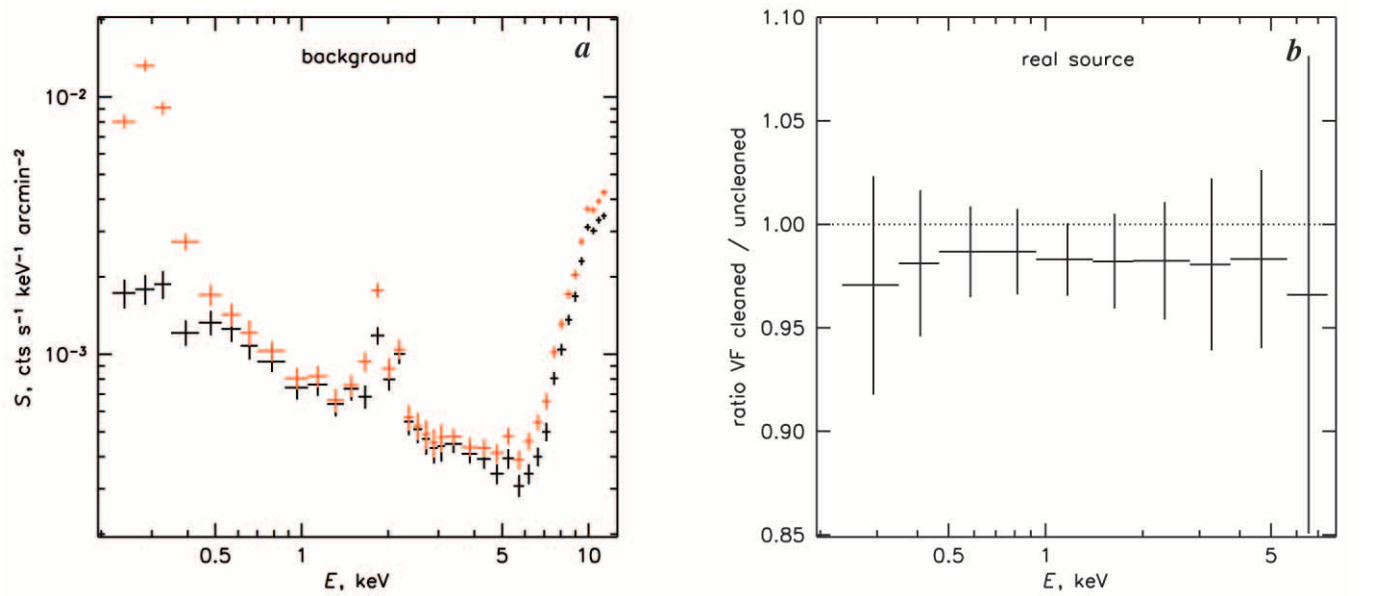

FIG. 8.—(*a*) Spectra of the S3 detector background (dark Moon) before (*red*) and after (*black*) VF mode cleaning. (*b*) Ratio of the spectra of a bright celestial source (without pileup) after and before VF mode cleaning. The noncosmic background is significantly reduced at low and high energies, while the effect on the real X-rays is energy-independent and very small.

In the three fields with pointlike original targets (ObsIDs 3013, 3419, and 930), we excluded $r = 30''$ circles around the target from the analysis. In ObsID 869, whose original target is a galaxy, we masked that source liberally and used the remaining 72% of the chip area.

Source detection was performed in two bands, 0.3–2 and 2–7 keV. The source candidates were identified in a standard manner, by applying wavelet filtering to the image to reduce statistical noise and then searching for local brightness maxima using the code of Vikhlinin et al. (1998). The source positions were then refined by photon centroiding and the source fluxes calculated within the 90% PSF–encircled energy radii r_{90} (and then divided by 0.9), using as the local background a wavelet decomposition component containing details on the largest angular scale. For simplicity, we set a relatively high, spatially uniform lower limit on the source flux that corresponds approximately to 8–10 photons anywhere in the field in each observation. This ensures that all detected sources are real and that the background contribution to the source flux is always small, even though we may miss some obvious fainter sources near the optical axis. As is seen below, these omissions do not affect our results significantly.

The resulting cumulative source counts from the 0.3–2 keV images as a function of the unabsorbed 0.5–2 keV source flux (assuming Galactic absorption and a power law with a -1.4 photon index for the source spectrum, relevant for the faintest sources) are presented in Figure 9. The figure also shows fits to the low-flux end of the 0.5–2 keV source counts from much deeper observations of *Chandra* Deep Field North (CDF-N; Brandt et al. 2001) and South (CDF-S; Rosati et al. 2002), which used the same assumption about the average source spectrum. Our curves are in good agreement with those results. The field-to-field difference (a factor of $\sim$2) is also similar to that between CDF-N and CDF-S (see also Barcons, Mateos, & Ceballos 2000), although with such low absolute source numbers that this result is not particularly significant.

For the interpretation of our diffuse measurements, it is useful to estimate the expected contribution of point sources below our detection limits. Figure 10 shows the cumulative 0.3–2 keV flux of all sources above a certain flux, divided by the total CXB signal in each observation (the total flux minus the Moon background; this quantity is different in all observations, being higher for ObsIDs 869 and 930). We can extrapolate these curves below our limits assuming, for

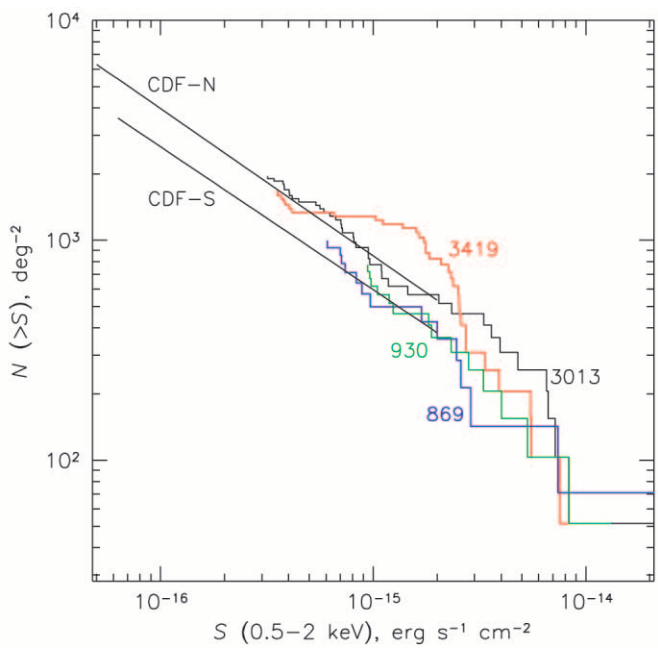

FIG. 9.—Cumulative numbers of excluded point sources as a function of their 0.5–2 keV flux. Only the sources detected in the 0.3–2 keV band are shown. Labels give ObsIDs. The curves end at our adopted lower flux cuts, which approximately correspond to 8–10 photons from the source. For comparison, low-flux fits to the CDF-N (Brandt et al. 2001) and CDF-S (Rosati et al. 2002) source counts are shown.

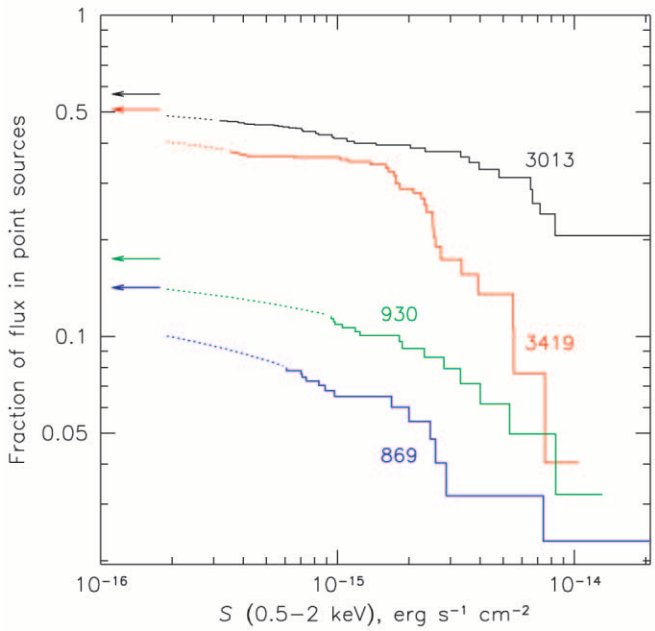

FIG. 10.—Contribution of the detected point sources above a certain flux to the total 0.3–2 keV count rate (minus detector background), as a function of the source 0.5–2 keV flux. Labels give ObsIDs. Dotted lines show extrapolations toward lower fluxes, assuming source counts as in CDF-N (Fig. 9); arrows indicate their asymptotic limits at zero flux.

example, the faint source distribution from CDF-N, as shown in the figure. The arrows show the asymptotic limits of those extrapolations at the zero flux. One can see that at most 60% of the 0.3–2 keV total CXB flux in our two main observations can be due to point sources (barring the emergence of an unknown source population at fluxes below the CDF limits or a significant change in the average source spectrum at the lowest fluxes; such possibilities are beyond the scope of this paper). The contribution of sources below our detection limits is less than 10% of the total CXB flux (and less than 20% of the unresolved flux) in all four observations; thus, the uncertainty of our extrapolation toward lower fluxes should not affect any of our conclusions.

At energies above 2 keV, the accuracy of our present measurements does not warrant a detailed analysis of the point-source contribution. Lists of sources detected in the 0.3–2 and 2–7 keV bands were merged, and circles of radius $2r_{90}$ around the sources ($3r_{90}$ for sources with more than 100 counts) were excluded from the spectral analysis below. Table 1 gives the resulting solid angles after the target and source exclusion.

5. SPECTRA AND INSTRUMENT RESPONSES

Diffuse CXB spectra were extracted in PI channels from the whole S3 chip, excluding the source regions. To extract the instrumental background spectra from exactly the same chip areas, we converted the dark-Moon event list into the corresponding sky coordinate frame using the aspect track of each CXB observation, assigning each Moon event a time tag selected randomly from the time interval spanned by that observation. The dark-Moon spectrum was then extracted from the same region specified in sky coordinates and normalized as described in § 3.2.3. All observations, including those of the Moon, are performed at the same focal plane temperature (−120°C), so the Moon spectra have the same resolution and can be directly subtracted from the CXB spectra.

A spectral redistribution matrix (RMF) for each observation was calculated by averaging the position-dependent matrices over the extraction region. Auxiliary response files (ARFs) included the telescope effective area and CCD quantum efficiency averaged over the extraction region. Regions of the masked sources were also excluded from the response averaging (this has any effect only for ObsID 869, for which a relatively large area is excluded). ARFs and RMFs were calculated using A. Vikhlinin's tools *calcarf* and *calcrmf*.

A recently discovered slow systematic decline of the ACIS quantum efficiency at low energies (Plucinsky et al. 2002) was taken into account in the ARFs. The present calibration accuracy of the quantum efficiency at $E \simeq 0.5$–0.7 keV is ~10%.

6. RESIDUAL BACKGROUND EXCESS

Our first-iteration spectra of the unresolved CXB from each observation are shown in Figure 11. For illustration, a 90% systematic uncertainty of the quiescent background normalization of ±3% is also shown. There is one more background correction that we need to perform. In our deepest observation, 3419, the diffuse spectrum above 2 keV is fully consistent with zero. In 3013, however, there is an obvious hard excess that cannot originate from the sky because of its unphysical spectrum. This is the excess discussed in § 3.1.1, where we proposed that it is a long flare of the same kind that affects the discarded time intervals in this observation, only fainter. Indeed, as the figure shows, the spectral shape of the hard excess is consistent with that of the flare model derived in § 3.1.1 (while being clearly inconsistent with an elevated quiescent background, for example). The model normalization was fitted to this spectrum in the 2.5–10 keV interval.

Thus, we proceed with the above assumption. The flare model also gives a significant contribution in the softer band. To correct it, we add this best-fit model to the detector background spectrum (this correction was already included in Fig. 10). Unfortunately, by doing so we are setting the diffuse flux above 2 keV in field 3013 to zero by definition, but such a correction is consistent with expectations from the light curve and the flare spectrum. A ±14% normalization uncertainty (1σ) of this flare model is included in the error budget for this observation.

Figure 11 also shows marginally significant excesses above 2 keV in ObsIDs 869 and 930, which can also be described by the flare model (for those fits, we adopted the parameters derived for the 930 flare in § 3.1.1). However, while the excess spectrum in 3013 does match the flare model, the same cannot be said with certainty for these two observations. The excesses are also comparable to the quiescent background uncertainty. As the figure shows, the possible flare contamination below 1 keV in these observations is negligible and can be safely ignored in the analysis below. However, the above discussion illustrates the difficulty of the diffuse CXB measurements at $E \gtrsim 2$ keV using the ACIS BI chip S3; FI chips may be better suited for that band (§ 8.4).

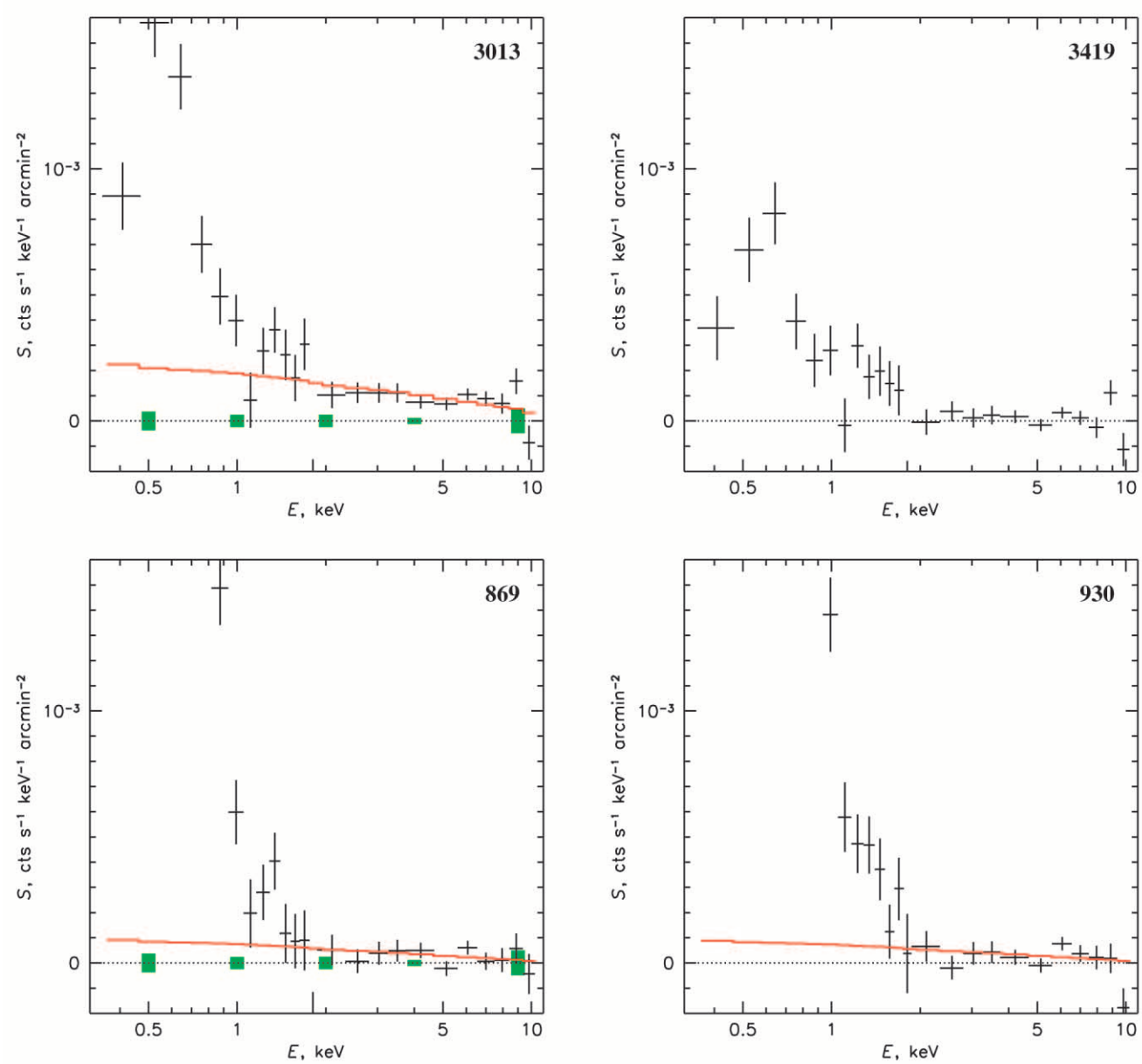

FIG. 11.—First-iteration spectra of the diffuse component for the four fields. ObsIDs are marked in each panel. For ObsIDs 3013, 869, and 930, models of the residual flares, whose normalizations were fitted in the 2.5–10 keV band, are shown as red histograms (see text). The soft flux in fields 869 and 930 is above the limit of the plots. Green bars illustrate the 90% quiescent background normalization uncertainty of ±3%. For 3013, the flare component is obvious and well described by the model; it is subtracted as an additional background component. For 869 and 930, it is marginally consistent with 0, given the background uncertainty. In all observations, the (possible) flare components are small compared to the diffuse signal in the soft band.

In the Appendix, we summarize the above background subtraction procedure and describe how it can be applied for other ACIS obsevations of extended sources.

7. RESULTS

Table 2 gives total and diffuse fluxes in our four CXB fields in three energy bands. It includes both the directly measured unresolved fluxes (that is, excluding the detected sources) and the estimated true diffuse fluxes after the small correction for undetected sources (see § 4 and Fig. 10). The 2–7 keV part of the table omits ObsID 3013 and the diffuse fluxes for ObsIDs 869 and 930 because of the residual background flare uncertainty (see § 6) that affects this band most significantly. The errors on these fluxes include statistical errors of the data and the Moon background and systematic uncertainties of the background. For ease of comparison with earlier results, Table 2 also gives the normalization of a power-law fit to the total spectra in the 1–7 keV band, with photon index fixed at −1.4 (a slope consistent with all four spectra, although only marginally so for field 930 because of a strong soft excess), assuming Galactic absorption. The average of the four fields is 10.7 ± 0.9 photons s^{-1} cm^{-2} keV^{-1} sr^{-1}. No attempt was made to correct our "total" fluxes for the missing very bright sources that we were unlikely to encounter because of the small field of view (covering a total of 0.07 deg^2), so these fluxes may not be representative of the sky average. The brightest sources found in our fields have unabsorbed 0.5–2 keV fluxes in the range $(1–5) \times 10^{-14}$ ergs s^{-1} cm^{-2}.

TABLE 2
WIDEBAND FLUXES

Flux	ObsID 3013	ObsID 3419	ObsID 869	ObsID 930
0.3–1 keV[a]				
Total	4.3 ± 0.2	2.2 ± 0.2	7.0 ± 0.2	7.8 ± 0.2
Unresolved	2.7 ± 0.2	1.6 ± 0.2	6.7 ± 0.2	7.4 ± 0.2
Diffuse[b]	2.4 ± 0.2	1.4 ± 0.2	6.4 ± 0.2	7.2 ± 0.2
1–2 keV[a]				
Total	1.1 ± 0.2	1.3 ± 0.2	1.0 ± 0.2	1.5 ± 0.2
Unresolved	0.3 ± 0.2	0.6 ± 0.15	0.7 ± 0.2	1.2 ± 0.2
Diffuse[b]	0.1 ± 0.2	0.3 ± 0.15	0.4 ± 0.2	1.0 ± 0.2
2–7 keV[a]				
Total	...	4.0 ± 1.5	4.7 ± 1.8	4.5 ± 1.5
Unresolved	...	1.6 ± 1.6	...	...
Diffuse[b]	...	0.8 ± 1.6	...	...
Power Law[c]				
Total	8.9 ± 1.6	12.1 ± 1.9	8.8 ± 1.6	12.8 ± 1.7

[a] In units of 10^{-15} ergs s^{-1} cm^{-2} $arcmin^{-2}$, uncorrected for absorption.
[b] Unresolved flux minus estimated contribution of undetected sources.
[c] Normalization of a power-law fit to the 1–7 keV total spectrum, corrected for absorption. Photon index is fixed at 1.4; $E = 1$ keV. Units are photons s^{-1} cm^{-2} keV^{-1} sr^{-1}.

Figure 12 shows relative contributions of different background components—instrumental, cosmic diffuse, and point sources—in our cleanest observation, 3419, which also has the lowest soft diffuse signal. Figure 13 shows the same spectra of the diffuse and total (including point sources) CXB after the instrumental background subtraction. Below 1 keV, a bright diffuse component dominates the CXB spectrum. In the 1–2 keV band, point sources dominate, continuing into the 2–5 keV band, where the diffuse component disappears.

Figure 14 shows the final diffuse spectra in the 0.25–1.2 keV band, with field 3013 corrected for the residual flare (see § 6). All exhibit a ubiquitous O VII feature around 570 eV (the He-like Kα blend), with possible contributions from Kβ at 665 eV and the O VIII Lyα line at 654 eV (these components cannot be resolved with the present statistics). The

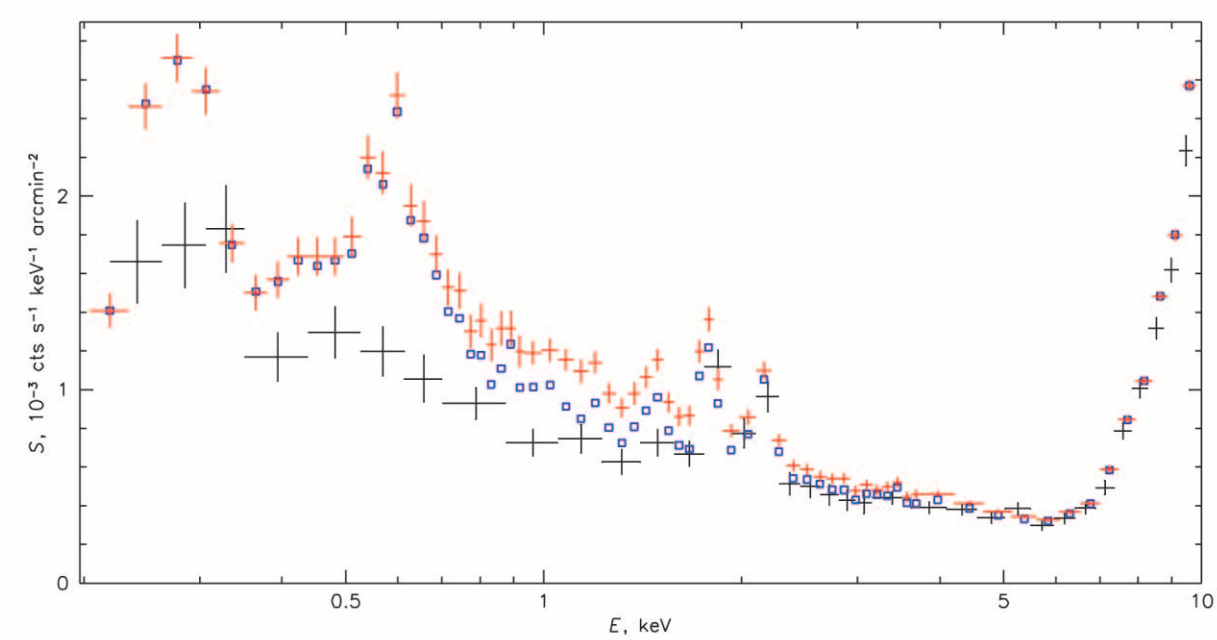

FIG. 12.—Spectra of ObsID 3419 (our field with the lowest diffuse signal) and the Moon background. Black crosses show the Moon renormalized to match the 10–12 keV rate of 3419 (see § 3.2.3). Red crosses show the total spectrum (excluding the target), and blue squares show the diffuse component after the exclusion of all point sources (blue error bars are similar to the red ones and are omitted for clarity).

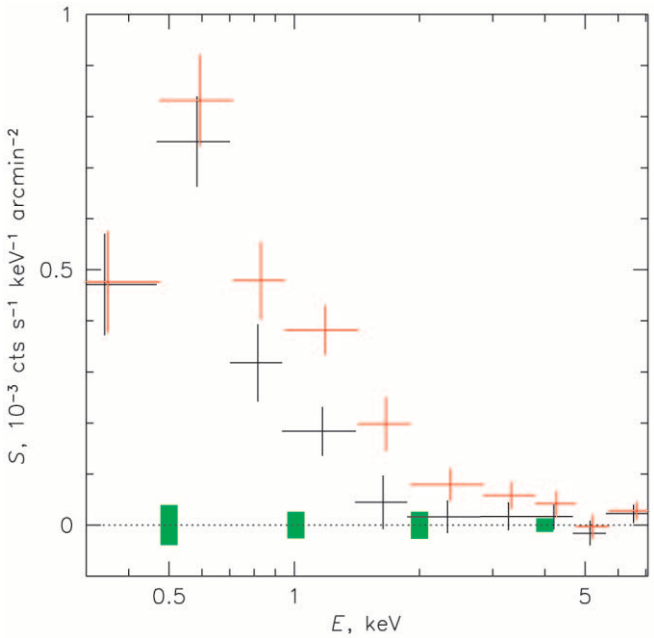

FIG. 13.—Spectra of ObsID 3419 after the detector background subtraction. Red shows the total spectrum and black shows the diffuse component from Fig. 12. Errors are dominated by the low statistics of the Moon. Green bars illustrate a 90% systematic uncertainty of the quiescent background normalization of ±3%. Above 2 keV, the diffuse component is consistent with zero.

best-fit mean energies and fluxes of this line blend are given in Table 3. The line brightness strongly increases in the direction of the North Polar Spur (fields 869 and 930), and an additional pair of bright features (around 730 and 820 eV, primarily from Fe XVII) emerges from the brighter part of the Spur (field 930). The lines are fitted well with a simple thermal plasma model (MEKAL; Kaastra 1992) with solar abundances, consisting of either one component (for the two fields off the Spur) or a two-temperature mixture (the Spur fields). The model parameters are given in Figure 14; the temperature range is 0.1–0.4 keV, and the best-fit absorption column is lower than the full Galactic value for all four observations. For ease of comparison, the best-fit models from Figure 14 are plotted together in Figure 15, taking away the time dependence of the ACIS efficiency.

There is also an apparent linelike feature at $E \sim 300$ eV, seen in all four spectra. Its brightness appears to change together with that of the O lines, and it is not present in the Moon spectrum (Fig. 12), which suggests that it is real. However, because of the present calibration uncertainties at the lowest energies, it is difficult to quantify its flux and even assess its reality. It should also be kept in mind that the same Moon spectrum with large statistical uncertainties was used as the background for all four observations.

8. DISCUSSION

8.1. *Comparison with Earlier Results*

We can compare our total (diffuse+sources) CXB results with the recent *XMM* work (Lumb et al. 2002). Since the brightest sources in our four fields have fluxes similar to the lowest fluxes of the excluded sources in Lumb et al. [$(1–2) \times 10^{-14}$ ergs s^{-1} cm^{-2} in the 0.5–2 keV band], our total fluxes can be directly compared with their values after the bright source exclusion. Starting from high energies, normalizations of our power-law fits in the 1–7 keV band given in Table 2 are in agreement with the *XMM* average of 8.4 photons s^{-1} cm^{-2} keV^{-1} sr^{-1} at 1 keV, if we exclude our bright field 930. In the narrower 1–2 keV band, our fluxes (again, except 930) are in good agreement with that of Lumb et al., 1.0×10^{-15} ergs s^{-1} cm^{-2} arcmin^{-2}, calculated from their best-fit model. Our 2–7 keV fluxes also agree with 3.2×10^{-15} ergs s^{-1} cm^{-2} arcmin^{-2}, converted from their 2–10 keV flux (we note here that these three values in Table 2 are not entirely statistically independent, because the error is dominated by the same Moon data set). Our uncertainties in the 2–7 keV band are large; future ways to reduce them are described in § 8.4.

Our 1–7 keV power-law normalizations also agree with 9–11 photons s^{-1} cm^{-2} keV^{-1} sr^{-1} at 1 keV, derived by Miyaji et al. (1998) from *ASCA* GIS data for two high Galactic latitude fields, and with 11.7 photons s^{-1} cm^{-2} keV^{-1} sr^{-1}, derived by Vecchi et al. (1999) using *BeppoSAX*. Note that those studies cover much greater solid angles and therefore are more likely to include rare, bright sources, so this comparison is only approximate.

At $E < 1$ keV, the scatter between our fields (a factor of 5) is higher than that in Lumb et al. (2002; a factor of 2–3), but this, of course, is because of our specific selection of fields spanning a range of *ROSAT* fluxes.

At the primary O-line energy, the CXB is dominated by the diffuse component (Fig. 13). Thus, we can compare our line fluxes with those recently derived, in a microcalorimetric experiment by McCammon et al. (2002), from a 1 sr area mostly away from bright Galactic features. They report an average flux in the O VII+O VIII lines of $(5.4 \pm 0.8) \times 10^{-7}$ photons s^{-1} cm^{-2} arcmin^{-2}. This is in the range of our values for the off-Spur observations 3013 and 3419 given in Table 3. McCammon et al. (2002) also observed lines at lower energies, some of which may explain our 300 eV feature (if it is real). Oxygen line fluxes derived from earlier

TABLE 3
OXYGEN LINE AND CONTINUUM FLUXES

ObsID	O-Line Energy (eV)	O-Line Flux[a] ($\times 10^{-7}$ photons s^{-1} cm^{-2} arcmin^{-2})	0.3–1 keV Continuum[b] ($\times 10^{-15}$ ergs s^{-1} cm^{-2} arcmin^{-2})
3013	570 ± 10	9.8 ± 1.5	3.2 ± 0.5
3419	580 ± 14	5.6 ± 1.5	3.5 ± 1.0
869	590 ± 6	15 ± 2	...
930	585 ± 8	12 ± 2	...

[a] Uncorrected for absorption.
[b] Flux excluding O-line, corrected for absorption assuming full Galactic column.

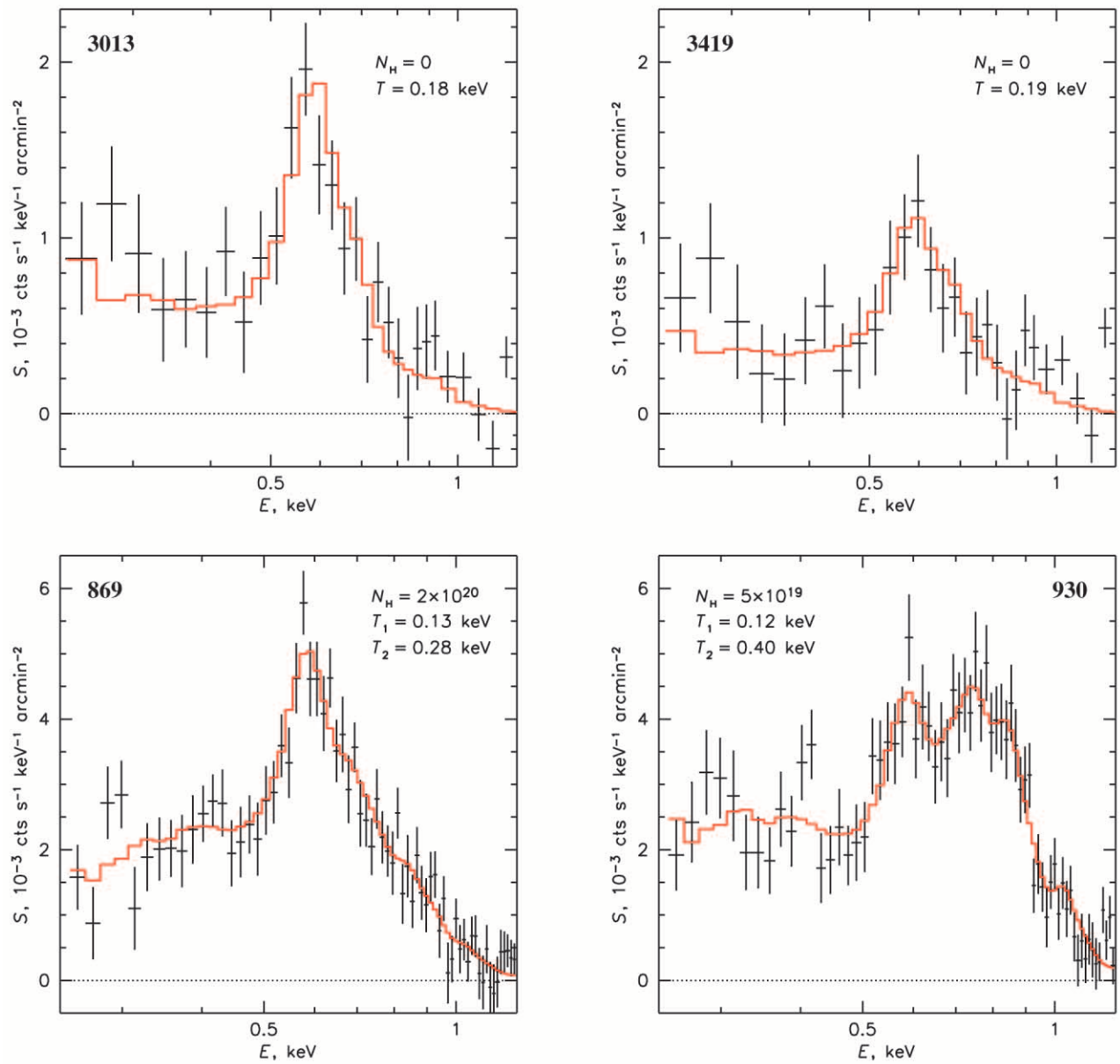

FIG. 14.—Final soft diffuse spectra. ObsIDs are marked in each panel. For 3013, the residual flare is subtracted (see Fig. 11). Histograms show simple one- or two-temperature thermal plasma fits, with parameters shown in the panels.

experiments (see, e.g., Inoue et al. 1979; Gendreau et al. 1995) are also within our range. Our results show, however, that even for these high Galactic latitude areas away from bright Galactic features, the line brightness varies significantly from field to field. The general shape of the North Polar Spur spectrum in our field 930 is consistent with that reported in earlier works (e.g., Schnopper et al. 1982; Rocchia et al. 1984; Warwick 2002).

8.2. *Extragalactic Diffuse Component*

The diffuse flux in fields 869 and 930 is obviously dominated by the North Polar Spur. The O blend in 3013 and 3419 probably has a Galactic or local origin as well (extragalactic sources with redshifts greater than 0.05 are excluded by our measured line energy; furthermore, the high-resolution spectrum of McCammon et al. 2002 excludes *any* redshift), although we cannot exclude, for example, its Local Group origin. Thus, the continuum component in the two low-brightness fields can give an approximate upper limit on the flux from the vast quantities of the putative warm intergalactic gas (see, e.g., Cen & Ostriker 1999) that should emit a mixture of lines and continua from different redshifts. For a conservatively high estimate of this continuum component, we fit the 0.3–1 keV diffuse spectra by a power-law model plus the line, applying the full Galactic absorbing column.

The resulting unabsorbed continuum fluxes are given in Table 3; they correspond to the spectral density of (2.4–2.5) $\times 10^{-15}$ ergs s^{-1} cm^{-2} arcmin^{-2} keV^{-1} at $E = 0.7$ keV. This is well above the typical theoretical predictions, which range between 0.3×10^{-15} and 10^{-15} ergs s^{-1} cm^{-2} arcmin^{-2} keV^{-1} (see, e.g., Cen & Ostriker 1999; Phillips, Ostriker, & Cen 2001, Voit & Bryan 2001; but see Bryan & Voit 2001 for a higher predicted flux from simulations without the inclusion of cooling and preheating). Note that the

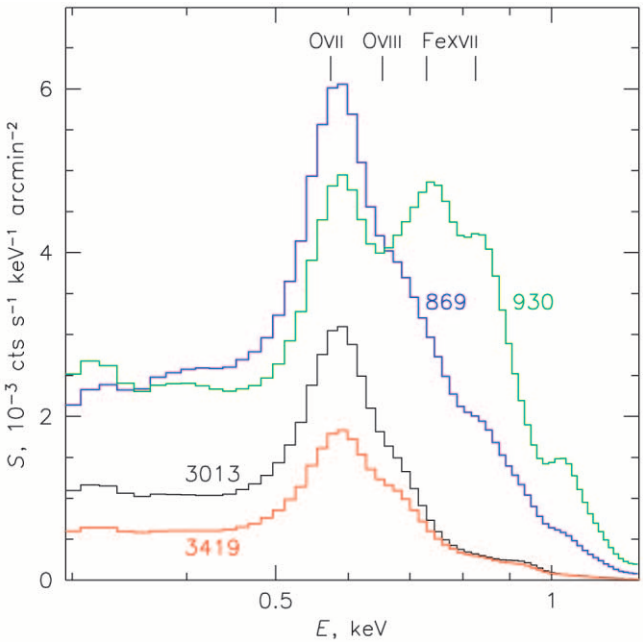

FIG. 15.—Model fits for different fields from Fig. 14. To be directly comparable, models are convolved with the same telescope response without taking into account its time change. ObsIDs and major line energies are marked.

predicted average brightness values from the published simulations are not directly comparable to our result, because they are dominated by nearby galaxy groups and clusters that are easily detected and excluded from our and other CXB measurements.

Thus, our crude estimate does not constrain the warm intergalactic gas models. The constraint may be improved in the future by better modeling and subtraction of the Galactic emission and spatial fluctuation analysis (as in, e.g., Kuntz, Snowden, & Mushotzky 2001); however, since the Galaxy dominates at these energies, such constraints will necessarily be model-dependent.

8.3. *Origin of Line Emission*

The observed energies of the spectral lines suggest local (in the Local Group, Galaxy, or our immediate vicinity) origin of the dominant fraction of the soft diffuse CXB. Extensive literature exists that models its various components under the well-justified assumption of their thermal plasma origin (see, e.g., Kuntz & Snowden 2000 and references therein). Leaving such modeling for future work, here we mention an interesting alternative possibility.

It is likely that a significant fraction of the line flux comes from charge exchange (CX) between highly charged ions in the solar wind (primarily bare and hydrogenic O and C) and neutral gas occurring throughout the heliosphere and in the geocorona. Most of the flux that would be observed from heliospheric CX (with H and He) originates within a few tens of AU of the Sun. Geocoronal emission arises where residual atmospheric H is exposed to the solar wind, at distances of the order of 10 Earth radii.

In the CX process, a collision between a solar wind ion and a neutral atom leads to the transfer of an electron from the neutral species to a high-n energy level in the ion, which then decays and emits an X ray. Dennerl, Englhauser, & Trümper (1997) and Cox (1998) were the first to suggest that these photons might contribute to the CXB, and Cravens (2000) estimated that heliospheric emission might account for roughly half of the observed soft CXB. Cravens, Robertson, & Snowden (2001) also argued that the excess time-variable diffuse flux often observed by *ROSAT* was due to fluctuations in heliospheric and especially geocoronal CX emission, caused by "gusts" in the solar wind.

In the *Chandra* Moon observations, the heliospheric component will be blocked, but geocoronal emission should be present. We estimate, however, that the typical intensity of that signal, about a few times 10^{-8} photons s^{-1} cm^{-2} $arcmin^{-2}$ in O Kα (the strongest line), is smaller than the statistical uncertainties in our measurement. Note also that the geocoronal signature is not likely to be present in our net CXB spectra, since it is subtracted as part of the Moon spectrum. Heliospheric CX emission should be stronger and less time-variable than geocoronal emission and should be present in our spectra. We have constructed a numerical model, based on Cravens' (2000) work and similar to that described in Wargelin & Drake (2001, 2002), that predicts that roughly half the flux in the O line(s) in fields 3013 and 3419 may come from heliospheric CX. Those observations were at low ecliptic latitude, within the "slow" and more highly ionized solar wind. CX flux in fields 869 and 930 is expected to be much lower, because those observations looked through the "fast" solar wind, which has a much smaller fraction of bare and H-like O ions (von Steiger et al. 2000). Observations of a sample of fields selected specifically to test this possibility are required for a more quantitative analysis, which is forthcoming (B. J. Wargelin et al. 2003, in preparation).

8.4. *Future Work*

For further CXB studies with *Chandra*, it is useful to look into the error budget of the present results. The errors in the 1–7 keV band are dominated by the detector background uncertainty: the statistical error of the short Moon data set, the uncertainty on its normalization, and the possible residual flare component. Forthcoming calibration observations with ACIS stowed but working in the full imaging mode should take care of the first component. The other two point toward the use of FI chips for studies in this band. The scatter of the quiescent background normalization probably cannot be reduced below our 2%–3% estimate; however, the FI detector background itself is lower by a factor of 2–3, depending on the energy. The FI chips also are much less affected by the background flares. An ACIS-I study of the CXB will be presented in a forthcoming paper (S. Virani et al. 2003, in preparation).

9. SUMMARY

We have analyzed four high Galactic latitude, empty fields observed with *Chandra* ACIS-S3 and, for the first time, derived spectra of the diffuse X-ray background, directly excluding the point-source contribution. The total (diffuse and point-source) CXB brightness in all bands is in agreement with most previous experiments. In the 0.3–1 keV band, the diffuse signal varies strongly between all four fields. In the two fields far from known bright Galactic features, it contributes about half of the total CXB seen by instruments with poorer angular resolution. It is dominated

by emission lines (most prominently, the O VII+O VIII blend at $E \approx 580$ eV, indications of which were also seen in previous experiments) and can be described by a thermal plasma model with $kT = 0.1$–0.2 keV. The line brightness increases strongly, and additional lines appear, in the directions of the North Polar Spur.

At higher energies, the background is more uniform. Diffuse emission is detected with high significance in the 1–2 keV band in the brighter of the two North Polar Spur fields. In other fields at $E > 1$ keV, the diffuse component is weak or consistent with zero at our present accuracy (to be improved in the forthcoming analysis of ACIS-I deep observations). Our current uncertainties for the diffuse CXB—one of the lowest surface brightness celestial objects—are large because of the difficulty of modeling the instrumental background in the time-variable particle environment encountered in high-altitude orbits like *Chandra*'s.

The results presented here are made possible by the successful effort of the entire *Chandra* team to launch and operate the observatory. We thank the referee for helpful comments and suggestions. Partial support was provided by NASA contract NAS 8-39073, grant NAG 5-9217, and the Smithsonian Institution.

APPENDIX

ACIS BACKGROUND SUBTRACTION

For the ACIS analysis of extended objects, the background can be modeled and subtracted as we did in § 3. In addition to the 2001 July–September dark-Moon data and the forthcoming observations with ACIS stowed that contain only the detector background, large data sets combining a number of high Galactic latitude, relatively source-free fields are available (see Markevitch 2001[8] for details). The latter data are cleaned of flares and point sources, but include the cosmic diffuse emission, so they are relevant when this emission is part of the background, as opposed to signal. Separate blank-sky data sets are assembled for three ACIS temperatures (which determine the spectral resolution) and for different time periods for the present $-120°$C temperature, to track the background evolution.

The following steps summarize our background subtraction procedure as it could be applied in a typical extended source analysis, using the combined blank-field data sets. In anomalous cases, this procedure may need more than one iteration.

1. To identify flares, we select a region of the chip(s) free of bright source emission and use it to create a light curve with time bins large enough to be able to detect rate changes by a factor of 1.2 (the fiducial factor used in creation of the blank-sky data sets). Using the relevant background data set (determined by the observation date), we evaluate the nominal count rate in the selected region and reject all intervals with the rate above a factor of 1.2 of this expected rate (usually, the flares are well defined in time and the exact threshold is not important). BI and FI chips should be cleaned separately, because BI chips are much more prone to flares. Given the spectra of the flares, for the BI chips, a 2.5–7 keV (or 2.5–6 keV for S1) energy band should be used, while for the FI chips, the full 0.3–12 keV band can be used.

If the target is in S3 and covers the whole chip, chip S1 can be used for flare detection. Despite the different quiescent backgrounds, S1 and S3 show a very similar response to flares, including the flare timing, spectra, and intensities. If S1 is not available either, then faint, nonobvious flares may escape detection and significantly affect the results, because flare and quiescent background components have very different spectral shapes (see, e.g., a discussion in Markevitch 2002 and § 3.1.1). In such cases, one should at least check the validity of the results by trying to fit a flare model to the spectrum above 2 keV extracted from low-brightness target areas (as in § 6). That spectral model applies only to the soft flare species that does not affect the FI chips.

If there is a faint, long flare in the observation whose proper exclusion results in too little useful exposure left, and if there are source-free areas in the chip of the same type, one can try to model the flare contribution using those areas (as was attempted in, e.g., Markevitch et al. 2002 and Markevitch 2002). However, the flare flux is not spatially uniform; its spatial distribution is under investigation.

2. After the flare exclusion, the background data set can be normalized by the ratio of high-energy rates, e.g., in the PHA interval of 2500–3000 ADU. This ratio should be within $\pm 10\%$ of the exposure ratio. Step 1 may need to be repeated with the corrected nominal rate if this correction is large. A 90% systematic uncertainty on the background normalization derived in this manner is about 3% (§ 3.2.3); however, if any residual faint flare is suspected, it should be taken into account in the final uncertainty.

3. If the observation was performed in VF mode, and if a VF mode background data set is available for that time period, additional background filtering (Vikhlinin 2001)[9] can be applied.

4. As seen from our results (e.g., Table 2), the soft ($E \lesssim 1$ keV) CXB component varies strongly from field to field even at high Galactic latitudes, so the blank-sky background may not have the correct soft spectrum. One can, for example, compare the RASS R4–R5 flux (Snowden et al. 1997) for a given observation to the average R4–R5 flux for the background data set to determine if a correction is needed (for low-b fields, it may be needed even if those wideband fluxes are similar, since the soft spectra may still be very different). If so, one can try to use regions of the field of view free of sources (not necessarily in the same chip) to model the sky soft excess or deficiency with respect to the blank-sky background (e.g., by the simple models used in this paper) and subtract this model from the regions of interest after the proper vignetting correction (as in, e.g., Markevitch & Vikhlinin 2001 and Markevitch 2002). An alternative is to use the dark-Moon data or the ACIS stowed data (if the observation date is sufficiently close to those data sets) and model away the whole diffuse CXB component.

[8] See http://asc.harvard.edu/cal, sections "ACIS," "Background," "General discussion."
[9] See http://asc.harvard.edu/cal, sections "ACIS," "Background," "VF mode."

REFERENCES

Baganoff, F. 1999, CXC ACIS background memo (Cambridge: CXC)
Barcons, X., Mateos, S., & Ceballos, M. T. 2000, MNRAS, 316, L13
Biller, B., Plucinsky, P., & Edgar, D. 2002, CXC ACIS background memo (Cambridge: CXC)
Brandt, W. N., et al. 2001, AJ, 122, 2810
Bryan, G. L., & Voit, G. M. 2001, ApJ, 556, 590
Bunner, A. N., Coleman, P. L., Kraushaar, W. L., McCammon, D., Palmieri, T. M., Shilepsky, A., & Ulmer, M. 1969, Nature, 223, 1222
Cen, R., & Ostriker, J. P. 1999, ApJ, 514, 1
Cox, D. P. 1998, in IAU Colloq. 166, The Local Bubble and Beyond, ed. D. Breitschwerdt, M. J. Freyberg, & J. Trümper (LNP 506; Berlin: Springer), 121
Cravens, T. E. 2000, ApJ, 532, L153
Cravens, T. E., Robertson, I. P., & Snowden, S. L. 2001, J. Geophys. Res., 106, 24883
De Luca, A., & Molendi, S. 2002, in New Visions of the X-Ray Universe in the *XMM-Newton* and *Chandra* Era (ESA SP-488; Noordwijk: ESA), in press (astro-ph/0202480)
Dennerl, K., Englhauser, J., & Trümper, J. 1997, Science, 277, 1625
Egger, R. J., & Aschenbach, B. 1995, A&A, 294, L25
Freyberg, M. J. 1998, in IAU Colloq. 166, The Local Bubble and Beyond, ed. D. Breitschwerdt, M. J. Freyberg, & J. Trümper (LNP 506; Berlin: Springer), 113
Garmire, G. P., Nousek, J. A., Apparao, K. M. V., Burrows, D. N., Fink, R. L., & Kraft, R. P. 1992, ApJ, 399, 694
Gendreau, K. C., et al. 1995, PASJ, 47, L5
Giacconi, R., Gursky, H., Paolini, F. R., & Rossi, B. B. 1962, Phys. Rev. Lett., 9, 439
Grant, C., Bautz, M., & Virani, S. 2002, in ASP Conf. Ser. 262, High-Energy Universe at Sharp Focus: *Chandra* Science, ed. E. M. Schlegel & S. D. Vrtilek (San Francisco: ASP), 401
Inoue, H., Koyama, K., Matsuoka, M., Ohashi, T., Tanaka, Y., & Tsunemi, H. 1979, ApJ, 227, L85
Kaastra, J. S. 1992, An X-Ray Spectral Code for Optically Thin Plasmas (Internal SRON-Leiden Rep., Version 2; Leiden: SRON)
Kamata, Y., Takeshima, T., Okada, T., & Terada, K. 1999, Adv. Space Res., 23, 1829
Kuntz, K. D., & Snowden, S. L. 2000, ApJ, 543, 195
Kuntz, K. D., Snowden, S. L., & Mushotzky, R. F. 2001, ApJ, 548, L119
Lumb, D. H., Warwick, R. S., Page, M., & De Luca, A. 2002, A&A, 389, 93
Markevitch, M. 2001, CXC ACIS background memo (Cambridge: CXC)
Markevitch, M. 2002, preprint (astro-ph/0205333)
Markevitch, M., Gonzalez, A. H., David, L., Vikhlinin, A., Murray, S., Forman, W., Jones, C., & Tucker, W. 2002, ApJ, 567, L27
Markevitch, M., & Vikhlinin, A. 2001, ApJ, 563, 95
Marshall, F. E., Boldt, E. A., Holt, S. S., Miller, R. B., Mushotzky, R. F., Rose, L. A., Rothschild, R. E., & Serlemitsos, P. J. 1980, ApJ, 235, 4
Marshall, F. J., & Clark, G. W. 1984, ApJ, 287, 633
McCammon, D., Burrows, D. N., Sanders, W. T., & Kraushaar, W. L. 1983, ApJ, 269, 107
McCammon, D., & Sanders, W. T. 1990, ARA&A, 28, 657
McCammon, D., et al. 2002, ApJ, 576, 188
Mendenhall, J. A., & Burrows, D. N. 2001, ApJ, 563, 716
Miyaji, T., Ishisaki, Y., Ogasaka, Y., Ueda, Y., Freyberg, M. J., Hasinger, G., & Tanaka, Y. 1998, A&A, 334, L13
Mushotzky, R. F., Cowie, L. L., Barger, A. J., & Arnaud, K. A. 2000, Nature, 404, 459
Phillips, L. A., Ostriker, J. P., & Cen, R. 2001, ApJ, 554, L9
Plucinsky, P. P., & Virani, S. N. 2000, Proc. SPIE, 4012, 681
Plucinsky, P. P., et al. 2002, Proc. SPIE, in press
Rocchia, R., Arnaud, M., Blondel, C., Cheron, C., Christy, J. C., Rothenflug, R., Schnopper, H. W., & Delvaille, J. P. 1984, A&A, 130, 53
Rosati, P., et al. 2002, ApJ, 566, 667
Sanders, W. T., Edgar, R. J., Kraushaar, W. L., McCammon, D., & Morgenthaler, J. P. 2001, ApJ, 554, 694
Schmitt, J. H. M. M., Snowden, S. L., Aschenbach, B., Hasinger, G., Pfeffermann, E., Predehl, P., & Trümper, J. 1991, Nature, 349, 583
Schnopper, H. W., et al. 1982, ApJ, 253, 131
Snowden, S. L., et al. 1995, ApJ, 454, 643
———. 1997, ApJ, 485, 125
Vecchi, A., Molendi, S., Guainazzi, M., Fiore, F., & Parmar, A. N. 1999, A&A, 349, L73
Vikhlinin, A. 2001, CXC ACIS background memo (Cambridge: CXC)
Vikhlinin, A., McNamara, B. R., Forman, W., Jones, C., Quintana, H., & Hornstrup, A. 1998, ApJ, 502, 558
Voit, G. M., & Bryan, G. L. 2001, ApJ, 551, L139
von Steiger, R., et al. 2000, J. Geophys. Res., 105, 27217
Wargelin, B. J., & Drake, J. J. 2001, ApJ, 546, L57
———. 2002, ApJ, 578, 503
Warwick, R. S. 2002, in New Visions of the X-Ray Universe in the *XMM-Newton* and *Chandra* Era (ESA SP-488; Noordwijk: ESA), in press (astro-ph/0203333)